Sequential Evaporation of Inverted $FAPbI_3$ Perovskite Solar Cells – Impact of Substrate on Crystallization and Film Formation

Alexander Diercks[a*], Julian Petry[b], Thomas Feeney[a], Roja Singh[a], Tonghan Zhao[b], Hang Hu[b], Yang Li[b], Ulrich W. Paetzold[a,b*], and Paul Fassl[a,b*]

[a] *Light Technology Institute, Karlsruhe Institute of Technology, Engesserstrasse 13, 76131 Karlsruhe, Germany*

[b] *Institute of Microstructure Technology, Karlsruhe Institute of Technology, Hermann-von-Helmholtz-Platz 1, 76344 Eggenstein-Leopoldshafen, Germany*

Corresponding authors

**alexander.diercks@kit.edu*

**ulrich.paetzold@kit.edu*

**paul.fassl@kit.edu*

Abstract

Recent advances in sequential evaporation of perovskite solar cells (PSCs) have culminated in a rapid increase in reported power conversion efficiencies (PCEs), now on par with the best solution-processed counterparts. This development triggered vast interest of industry and academics. To date, however, very few studies addressed sequentially evaporated PSCs in the *p-i-n* architecture and an in-depth process understanding is lacking. Here, we investigate the impact of the hole transport layer (HTL) on the formation of formamidinium lead triiodide (FAPI) perovskite thin films fabricated via an evaporated two-step process. We find that the crystal orientation of lead iodide (PbI_2) changes significantly for different HTLs, thereby impacting the subsequent conversion and crystallization process. Adjusting the amount of deposited FAI reveals an unexpected correlation of the PbI_2-to-perovskite X-ray diffraction peak intensity ratio to final PSC performance that depends on the employed HTL. Our approach enables PCEs of more than 17%, the highest reported for fully vacuum-processed pure FAPI PSCs in the *p-i-n* architecture.

TOC GRAPHICS

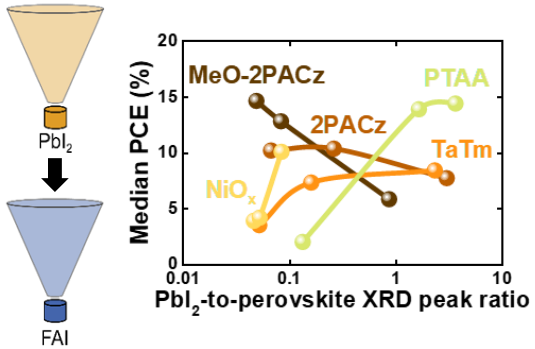

Organic-inorganic metal halide perovskite solar cells (PSCs) are one of the most promising options for next-generation photovoltaics, given their tunable band gap,[1,2] long charge carrier diffusion lengths,[3] defect tolerance, and high absorption coefficients.[4] The rapid increase in reported power conversion efficiencies (PCEs) over the past decade, with certified PCEs approaching 27%, made them serious competitors to established thin-film technologies such as copper indium gallium-selenide (CIGS) and cadmium telluride (CdTe).[5,6] Most research on PSCs has focused on solution-based fabrication methods of the perovskite absorber layer (*e.g.*, spin coating, inkjet printing, blade coating, and slot-die coating).[7] These processes allow for rapid and cost-effective process optimization and fast perovskite layer deposition. In contrast, less than 1% of all existing publications report on PSCs fabricated using vacuum-based thermal evaporation (TE) deposition processes even though they dominate today's established thin-film manufacturing.[8–10] Furthermore, TE offers conceptual advantages such as homogeneous deposition over larger areas and conformal coverage of textured surfaces for industrially relevant applications.[11–13] Most reports on TE employ a co-evaporation approach, in which all perovskite precursor materials are deposited simultaneously in a single deposition step. The first reports of co-evaporated PSCs in 2013 already achieved PCEs of up to 15.4%, employing methylammonium iodide (MAI) and lead chloride ($PbCl_2$) as precursors.[14] Since then, more complex compositions (*e.g.*, double-cation, triple-cation and mixed halides)[15–18] as well as more advanced processes (*e.g.*, faster deposition, multi-halide molten salts)[19–22] have increased our understanding of TE processes significantly. The current record PCE of co-evaporated PSCs reported by Leyden *et al.* in 2024 is 21%[23] – significantly below the values achieved for solution processing.[8] One reason for the limited PCE is that co-evaporated perovskite thin films exhibit a pronounced substrate dependency, complicating process optimization. There are several studies that address the complex impact of the substrates on perovskite formation during co-evaporation.[24–29] In our previous study, Abzieher *et al.* showed the effect of different HTLs on co-evaporated methylammonium lead triiodide (MAPI) perovskite thin film formation and correlated the observations to different surface polarities of the substrates.[27] Furthermore, interfacial interactions such as the formation of hydrogen bonds between phosphonic acid functional groups in case of self-assembled monolayer (SAM)-based HTLs and interfacial iodide anions impact reaction kinetics for co-evaporated formamidinium (FA)-based absorbers, resulting in increased organic incorporation rate and preferential α-$FAPbI_3$ growth.[24,25,29]

An alternative vacuum-based TE method is the sequential layer deposition process, where the precursor materials are deposited in two or more subsequent deposition steps. The first study by Chen *et al.* investigating this process employed $PbCl_2$ and MAI as precursor materials and achieved a decent PCE of 15.4% in 2014.[30] The following years exhibited increases in reported PCEs reaching up to 21.3% in 2021 for a $FA_xCs_{1-x}PbI_3$ absorber.[31–33] More recent studies by Yi *et al.* proved the great potential of the sequential layer deposition approach by reaching PCEs of 24.4% in 2023 and over 26% in 2024, closing the gap to solution-processed PSCs (see Figure 1b).[20,34,35] Various approaches have been reported, such as single-layer and alternating multilayer depositions, as well as the use of different material compositions of the perovskite layer, demonstrating the versatility and applicability of this fabrication approach.[31–33,36–38] However, most studies on the vacuum-based sequential layer deposition process focus on the *n-i-p* architecture,[20,31,32,34,36,38–43] while reports on the *p-i-n* architecture are heavily underrepresented (see Figure 1c and Table S1).[30,33,37,44,45] The *p-i-n* architecture displays several key advantages in the context of future applications, *e.g.*, facile integration into monolithic tandem PV devices and high operational stability, making further research and development crucial.[46–49] Decoupling the simultaneous co-evaporation of precursor materials into two or more subsequent deposition steps promises several advantages: (i) the ability to reduce cross-contamination and thus improve reproducibility since different evaporation chambers are used for each material, and (ii) the potential for high-throughput in-line processing using several linear

evaporators.[50] While the impact of the substrate on the crystallization of co-evaporated perovskites is well studied,[24,27,28] the interplay between the substrate and the quality of sequentially evaporated perovskite thin films has not been investigated yet.

In response, this work investigates the effect of different HTLs on the formation of formamidinium lead triiodide (FAPI) perovskite thin films fabricated via an evaporated two-step process. We observe significant differences in the morphology and crystallinity of the films, impacting the performance of resultant FAPI PSCs in the *p-i-n* architecture. To identify the reason for this, we analyze the firstly deposited PbI_2 layers using scanning electron microscopy (SEM), atomic force microscopy (AFM), and grazing-incidence wide-angle X-ray scattering (GIWAXS) measurements. We find a strong impact of the HTL on the morphological properties of the PbI_2 layer and reveal a significant change in crystal orientation, which subsequently affects the conversion to the perovskite phase after deposition of FAI. To further investigate the relationship of different PbI_2 structural properties and conversion to the final perovskite phase, we adjust the FAI to PbI_2 stoichiometry and find an unexpected correlation of the X-ray diffraction (XRD) pattern and final PSC performance that serves as a guideline for PCE optimization on different HTLs. Finally, we show the possibility of manipulating the observed structural properties by adjusting process parameters (evaporation rate and substrate temperature) during the deposition of the PbI_2 layer. We achieve PCEs of up to 17.2% (stabilized at 16.0%) for a fully vacuum-processed pure FAPI perovskite composition, the highest reported number in the *p-i-n* architecture. In summary, this work provides an in-depth understanding of the effect of substrate for the vacuum-based sequential evaporation process and emphasizes the difficulty to analyze and compare 2D XRD patterns of the same perovskite composition on different HTLs.

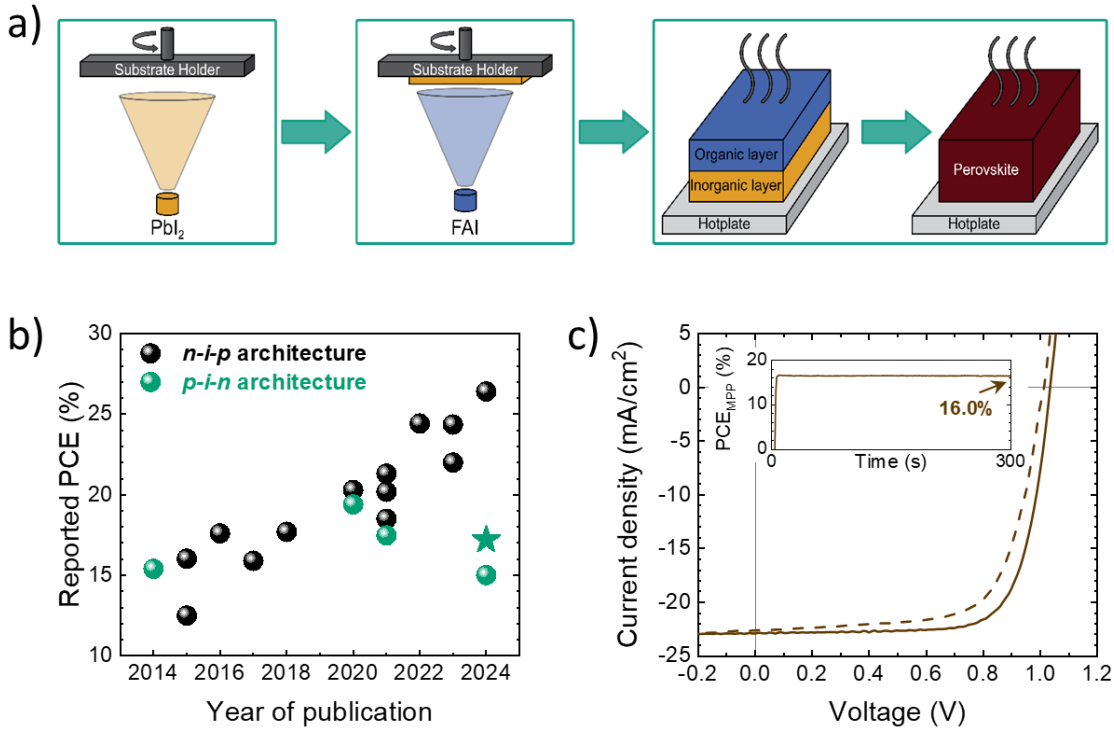

Figure 1: a) Schematic of the sequential layer deposition process. b) Published champion PCE values of sequential layer deposition processes (see more details in Table S1). The star represents the champion PCE presented in this work c) J-V analysis and MPP-tracking of the champion device with the layer sequence ITO/evaporated MeO-2PACz/perovskite/C60/SnOx/Ag.

Vacuum-based sequential layer deposition of perovskite thin films encompasses a wide range of deposition sequences. Existing reports vary from subsequent single-material layer depositions to alternating multilayer deposition processes, as well as processes using co-evaporated intermediate steps.[30–34,36–38,51,52] The various reported processes and resulting photovoltaic parameters are summarized in Table S1. Here, we apply an evaporated two-step process to fabricate FAPI PSCs in the *p-i-n* architecture as schematically depicted in Figure 1a. In the first evaporation step we deposit the PbI_2 layer, followed by the deposition of FAI in the second evaporation step (see Experimental Section in the SI for further details). Both deposition processes are carried out in dedicated evaporation chambers to avoid cross-contamination. Conversion to the final perovskite phase happens during an annealing step at 170 °C for 15 min under ambient atmosphere (~30-40% relative humidity), with humidity enhancing diffusion of the organic cations.[34,43,52] The *J-V* characteristics of the best performing PSC are displayed in Figure 1c. It consists of the layer stack glass/ITO/MeO-2PACz/$FAPbI_3$/C_{60}/ALD-SnO_x/Ag, using our recently developed evaporated MeO-2PACz SAM-HTL (from now on referred to as MeO).[53] The PCE in the reverse scan is 17.2% (J_{SC} = 22.9 mA/cm^2, V_{OC} = 1.01 V, FF = 74.2%) with a stabilized PCE of 16.0%, the highest reported PCE of fully vacuum-processed FAPI PSCs in the *p-i-n* architecture.

To test whether differences in perovskite film formation on different HTLs occur, we investigated sequentially evaporated perovskite thin films (after annealing) by analyzing SEM and XRD measurements. The five chosen HTLs (MeO, 2PACz, TaTm, NiO_x, and PTAA) are widely used in literature and exhibit notable differences in their chemical properties. We observe changes in the average grain size of the perovskite thin film as depicted in representative SEM images in Figure 2a. Specifically, films on MeO and 2PACz exhibit more disoriented and smaller grains, while the average grain size is larger on TaTm, NiO_x and PTAA, which can also be seen in the corresponding cross section images (Figure S1). This indicates that the underlying substrate directly impacts the morphology of sequentially evaporated perovskite thin films. XRD analysis of the films further supports this interpretation. Perovskite layers on all HTLs show a different ratio of the (100)-PbI_2 to (001)-perovskite peak intensities (from now on referred to as PbI_2-to-PVK peak ratio), indicating a change in the crystallization and conversion process to the perovskite phase (Figure 2b). In addition, the performance of completed PSCs differs significantly, with no correlation to the observed differences in XRD patterns (Figure 2c, Figure S2 and Figure S3). In literature, often a beneficial effect of small or even significant amounts of residual PbI_2 in the perovskite film is observed, independent of the employed HTL/ETL.[54,55] In our case, PCEs of PSCs on MeO reach median values of around 15% with a negligible PbI_2-to-PVK peak ratio, similar to those obtained in case of PTAA as HTL which, however, exhibits the highest PbI_2-to-PVK peak ratio from XRD. This reveals that the comparison of XRD patterns of perovskite thin films on different HTLs is not a reliable indicator for the performance of complete PSCs. We note that the different HTLs themselves can have an impact on device performance due to variations in non-radiative interfacial recombination and selective hole transport.[56,57] However, it is reasonable to assume that the observed differences mainly depend on a substrate-dependent perovskite film formation and its impact on resulting film quality. Therefore, the latter is the main subject of investigation in this study.

The key difference of the two-step evaporation process as compared to its co-evaporation counterpart is the formation and crystallization process of the perovskite phase. In case of co-evaporation, all precursor materials make contact with the substrate simultaneously, leading to immediate formation of perovskite nano crystallites at the interface with the substrate during deposition.[27,58] As discussed above, co-evaporation processes are therefore known to be strongly affected by the underlying substrate, resulting in the need for an optimization of process parameters to each substrate to form perovskite films of comparable quality.[27] In contrast, perovskite film formation and crystallization in

case of the evaporated two-step process starts at the interface between the subsequently evaporated inorganic and organic materials, and full crystallization to the perovskite phase is only achieved during the annealing step in which the inorganic and organic parts are intermixed by diffusion. Thereby, a much smaller dependence of perovskite crystal growth on the substrate is expected.

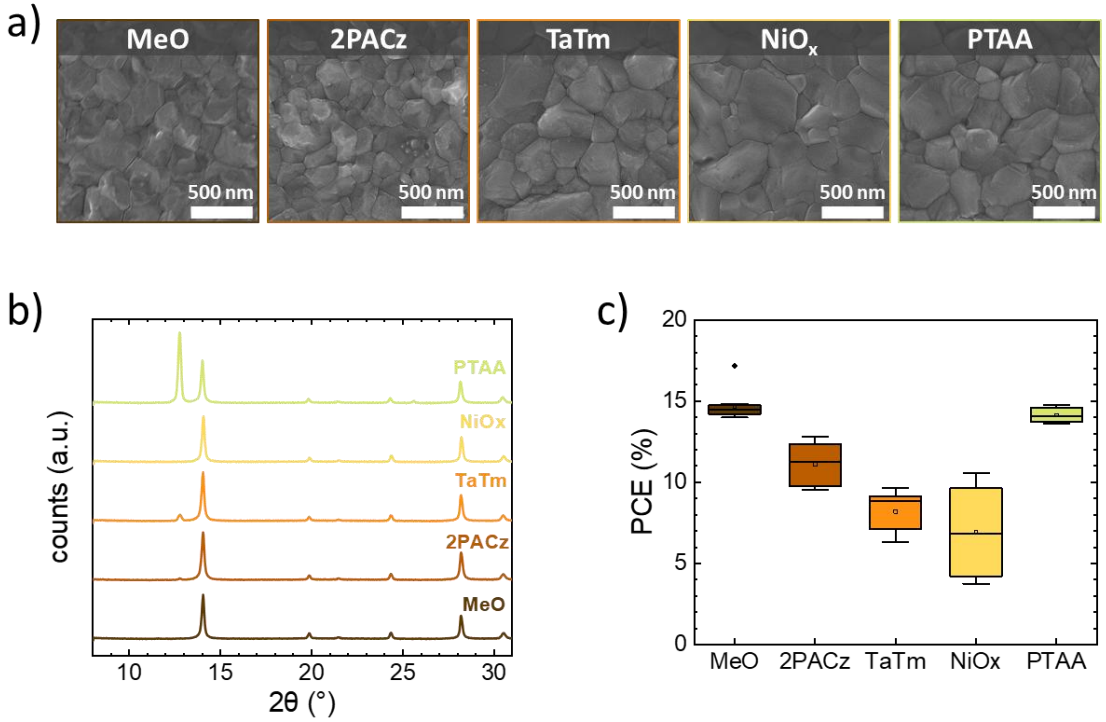

Figure 2: a) Scanning electron microscopy surface images of perovskite thin films on different HTLs. b) X-ray diffraction patterns of perovskite thin films on different HTLs. c) PCE statistics of final PSCs.

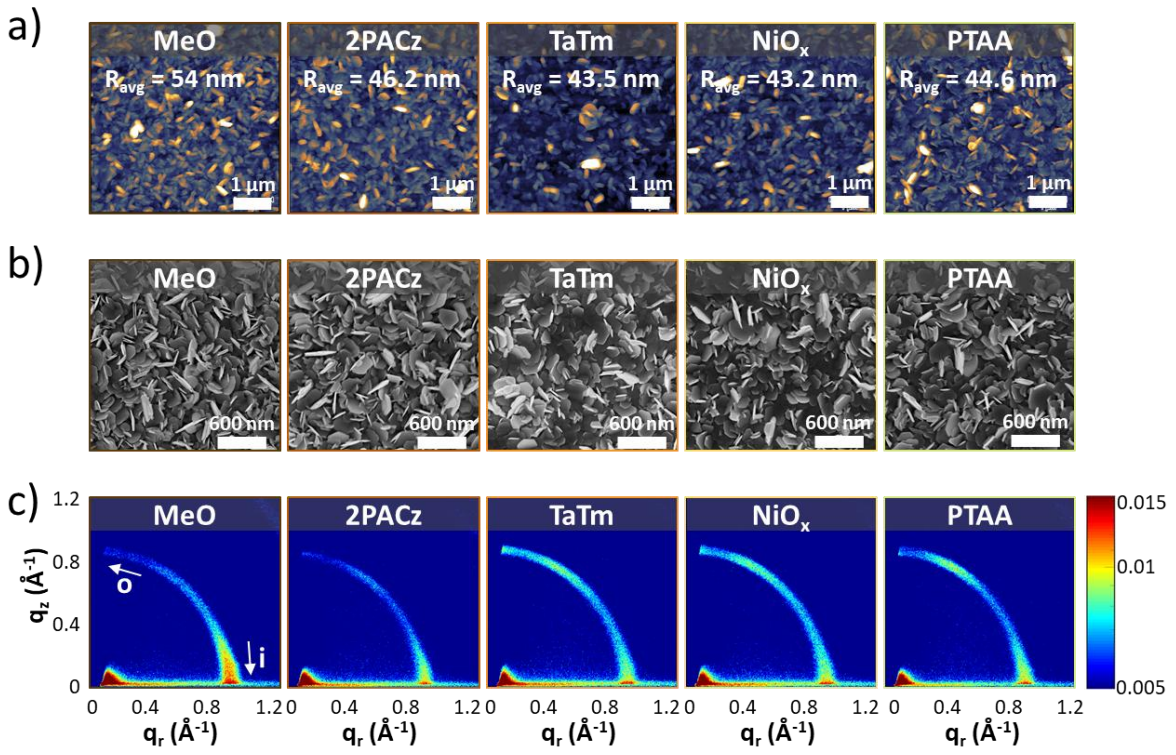

Figure 3: a) Atomic force microscopy analysis of evaporated PbI_2 layers on different HTLs with average surface roughness values. b) Scanning electron microscopy images of evaporated PbI_2 layers on different HTLs. c) GIWAXS analysis of evaporated PbI_2 layers on different HTLs. "o" denotes out-of-plane orientation, "I" denotes in-plane orientation of the crystallites.

To understand the impact of different substrates on perovskite formation in greater detail, we next analyzed the inorganic layer morphology and microstructure. From AFM measurements of the PbI_2 thin films, we find that the surface roughness (R_{avg}) on the different HTLs varies from R_{avg} = 43.2 nm in case of NiO_x to R_{avg} = 54 nm in case of MeO (see Figure 3a). A higher R_{avg} results in a larger surface area of the PbI_2 layer that is in contact with the subsequently deposited FAI. A larger contact area could simplify interdiffusion of FAI into the inorganic scaffold and accelerate the initial conversion reaction of the two precursor materials. Furthermore, in the case of dry-wet hybrid two-step deposition processes, rougher films are often considered to be more porous which facilitates the interdiffusion of the organic cations into the inorganic scaffold.[59,60] However, the differences in R_{avg} between 2PACz, TATm, NiO_x and PTAA are comparatively small, despite strong differences in final perovskite film properties and device performance, requiring more in-depth analysis. Next, we analyzed SEM images of the evaporated PbI_2 thin films on the different substrates. We observe slight changes in the orientation of the PbI_2 platelets depending on the underlying substrate (see Figure 3b and Figure S4). On MeO and 2PACz, the PbI_2 platelets appear to be more vertically oriented, which is in line with a slightly higher R_{avg} from the AFM measurements. PbI_2 layers on TaTm, NiO_x and PTAA appear to have more horizontally orientated PbI_2 platelets. We can conclude that the morphological properties, especially the orientation of the PbI_2 platelets are affected by the underlying substrate. Yet, there seems to be no clear correlation between morphological properties and final PSC performance. To further analyze the effect of different substrates on the microstructural properties of the inorganic layer, we performed GIWAXS measurements of the evaporated PbI_2 thin films. GIWAXS can give information on different crystal growth orientations and the overall degree of crystallinity of thin films.[61] PbI_2 layers on all HTLs show an intensity maximum in an in-plane orientation (referred to as "i" in Figure 3c), indicating the (001)-plane of PbI_2 is perpendicular to the substrate surface. Whereas

for PbI_2 layers on MeO and 2PACz HTLs we do not detect another intensity maximum, PbI_2 layers on TaTm, NiO_x and PTAA show a second preferred orientation in a more out-of-plane orientation (referred to as "o" in Figure 3c), meaning a more vertically (001)-oriented growth. The corresponding pole figures with integrated intensity over corresponding azimuth angle are shown in Figure 4a. It has been reported previously that the crystal orientation of the PbI_2 layer can affect the diffusion of organic cations, both for the hybrid deposition and sequential evaporation processes, and therefore impact the conversion reaction during the annealing step.[34,62–66] Yi *et al.* proved that a preferred orientation of the evaporated lead iodide-chloride layer strongly affects the conversion and quality of their sequentially evaporated perovskite films.[34] However, substrate-dependent growth and the impact on crystal orientation of evaporated PbI_2 layers has not yet been investigated. More out-of-plane orientation, meaning more vertically oriented PbI_2 crystals, might facilitate the penetration and diffusion into the inorganic layer during the deposition of the organic cation and the subsequent annealing step. To summarize, the choice of substrate has a significant impact on the crystal growth of the inorganic layer deposited in the first step. This is evident from morphological changes such as grain size and surface roughness as well as the crystal orientation of the PbI_2 layer.

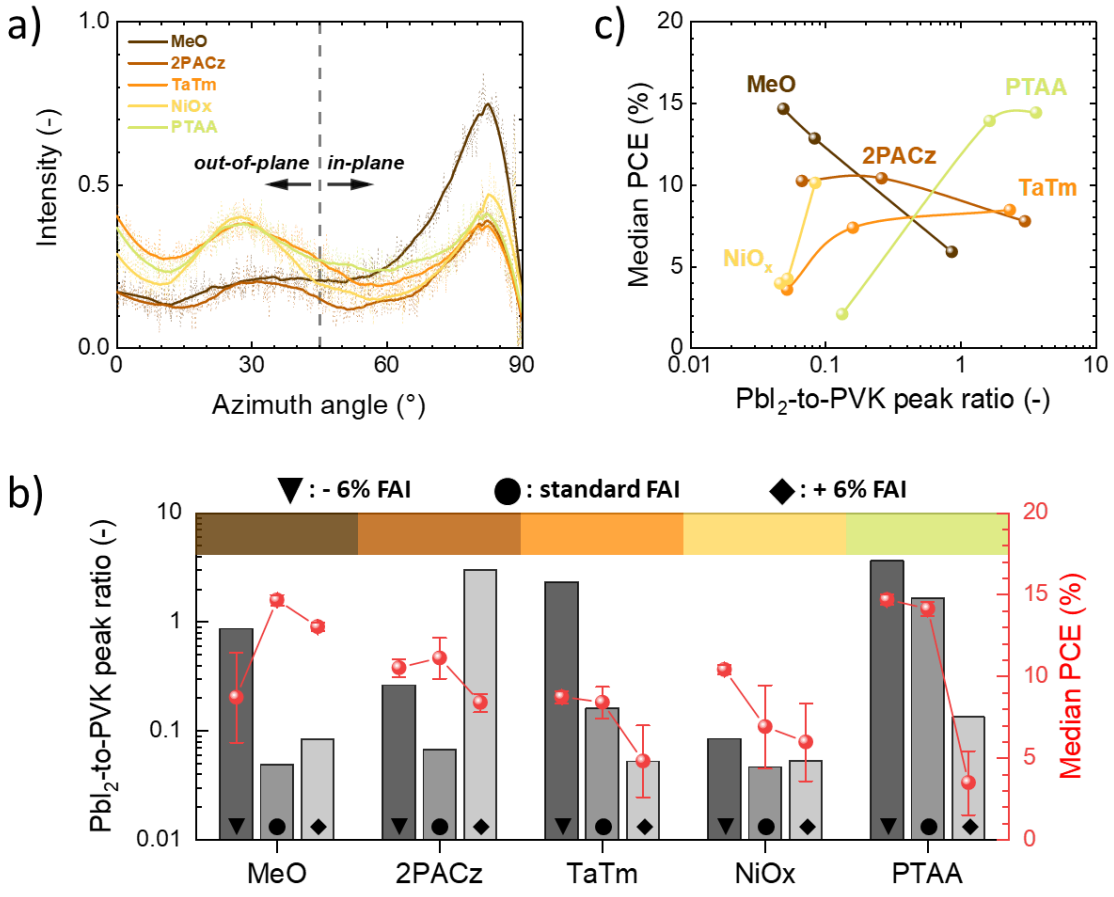

Figure 4: a) Pole figures from GIWAXS measurements of evaporated PbI_2 layers on different HTLs. b) Guideline plot for maximum median PCE of FAPI PSCs on different HTLs depending on PbI_2 to perovskite XRD peak intensity ratio. c) XRD peak-ratio evolution for different FAI to PbI_2 ratios (increasing from left to right: -6%, standard, +6%) with corresponding median PCEs. Standard refers to film thicknesses for PbI_2 and FAI of 300 nm and 280 nm respectively.

Next, by altering the stoichiometry of FAI to PbI_2 by adjusting the amount of deposited FAI, we reveal that the crystal orientation of the evaporated PbI_2 layer on different HTLs has a direct and unexpected impact on the conversion and crystallization process as well as the photovoltaic parameter of complete PSCs. When reducing the deposited FAI layer thickness from the standard value to -6%, we find an increased XRD PbI_2 intensity and PbI_2-to-PVK peak ratio for all studied HTLs (see Figure S5). Notably, an increase in the deposited FAI amount (+6%) shows different trends for the various HTL that seem to depend on the PbI_2 crystal orientation. Films on MeO and 2PACz with more in-plane PbI_2 orientation show an increased PbI_2-to-PVK peak ratio, in stark contrast to the expectation. PbI_2 layers with increased out-of-plane orientation show the reverse trend, leading to a further reduction of the PbI_2-to-PVK intensity ratio (see Figure 4b). Pairing these films with median PCE values of the resulting PSCs reveal a significant difference between optimum PbI_2-to-PVK peak ratio and resulting PCE (see red data points in Figure 4b, for full statistics see Figure S6), resulting in a direct correlation to the previously observed PbI_2 crystal orientation. PSCs on MeO and 2PACz, which show a more in-plane orientation of the firstly evaporated PbI_2 layer, display their best performing devices for a lower PbI_2-to-PVK peak ratio. In contrast, PSCs on TaTm, NiOx and PTAA, showing more out-of-plane oriented PbI_2 crystals, yield the best results for higher relative intensities of PbI_2 in their XRD patterns (see Figure S5 and Figure S6). By plotting median PCEs over the corresponding PbI_2-to-PVK peak ratios we obtain a guideline plot showing general trends for the fabrication of sequentially evaporated PSCs and their preferred regime for optimum performance on different HTLs (see Figure 4c).

Given the importance of morphological and microstructural properties of the PbI_2 layer on the conversion to the perovskite phase, we sought to further investigate how to manipulate these properties by changing process parameters, more specifically deposition speed and substrate temperature. We chose to vary the evaporation rate of PbI_2 in the range of 0.1 Å/s to 2.0 Å/s and the temperature of the substrate (5 °C, 20 °C, 45 °C, and 70 °C) and employ MeO as SAM-HTL since it yielded the best device performance. Changing the substrate temperature for a constant PbI_2 evaporation rate of 1.0 Å/s has no major effect on the crystal orientation of the inorganic scaffold (see Figure S7a). As shown in the pole figures of the GIWAXS measurements, all layers exhibit a similar single orientation maximum in a more in-plane orientation (see Figure 5a). In contrast, different PbI_2 evaporation rates with a constant substrate temperature of 20 °C exhibit a clear effect on crystal orientation (see Figure S7b). While an increase in evaporation rate to 2.0 Å/s leads to a more strongly pronounced in-plane growth of the PbI_2 crystallites, slower deposition speeds display a second orientation maximum in an out-of-plane orientation (see Figure 5a). Additionally, with top view SEM images we see that both process parameters, deposition speed and substrate temperature, affect the apparent grain size of the evaporated PbI_2 layers. While slower evaporation rates result in larger PbI_2 platelets, an increase in substrate temperature leads to a decrease platelet size (see Figure S8). Both process parameters therefore do have an impact on the morphological and microstructural properties of the evaporated PbI_2 layer.

To confirm the previous findings, we used the differently processed PbI_2 layers for our evaporated two-step process to analyze the conversion to perovskite as well as the final PSC performance. After the deposition of FAI and subsequent annealing, we detect strong differences in the final XRD patterns, especially regarding the PbI_2-to-PVK peak ratio (see Figure 5b and Figure S9). The corresponding PCEs of the resulting PSCs confirm the earlier findings and are in line with the general XRD trends of our perovskite layer on MeO (compare Figure 4c). High PbI_2-to-PVK peak ratios from XRD analysis of the perovskite layer result in decreased PCEs of the corresponding PSCs, while low PbI_2-to-PVK peak ratios generally result in improved performance (see Figure 5c and Figure S10). We hereby show that it is possible to manipulate the growth and final properties of the evaporated inorganic layer simply by adapting easily accessible process parameters (deposition speed and

substrate temperature) during evaporation. We observe the same trends for XRD and PSCs performance that we observed on various HTLs, underlining the validity of our guideline plot in Figure 4c.

In this work, for the first time, we reveal a substrate-dependent film formation of $FAPbI_3$ perovskite thin films fabricated with an evaporated two-step process. We show that the substrate affects the morphological and microstructural properties of the firstly evaporated PbI_2 layer, which impacts the conversion to perovskite after deposition of FAI and the corresponding PSC performance. Changes in crystal orientation of the PbI_2 layer as measured by GIWAXS are found to affect the PbI_2-to-PVK XRD peak intensity ratio that shows an unexpected trend, revealing that analysis of the PbI_2 peak intensity is not a reliable solar cell performance indicator. Based on these findings, we provide a guideline for XRD analysis to achieve the highest performing PSCs on different HTLs based on coupled GIWAXS and XRD analysis. Furthermore, we studied the effect of variation in process parameters on the PbI_2 layer properties and show the possibility to manipulate the PbI_2 crystal orientation by adjusting the deposition speed. Using this approach, we fabricated highly efficient MA-free PSCs in the *p-i-n* architecture with PCEs of up to 17.2% (stabilized at 16.0%). This represents not only the first MA-free PSCs in the *p-i-n* architecture using an evaporated two-step process, but also the highest reported PCE for fully vacuum-processed pure FAPI PSCs. Our work further provides an in-depth understanding of the sequential layer evaporation deposition process and paves the way to highly efficient PSCs using an industrially relevant and highly promising fabrication method.

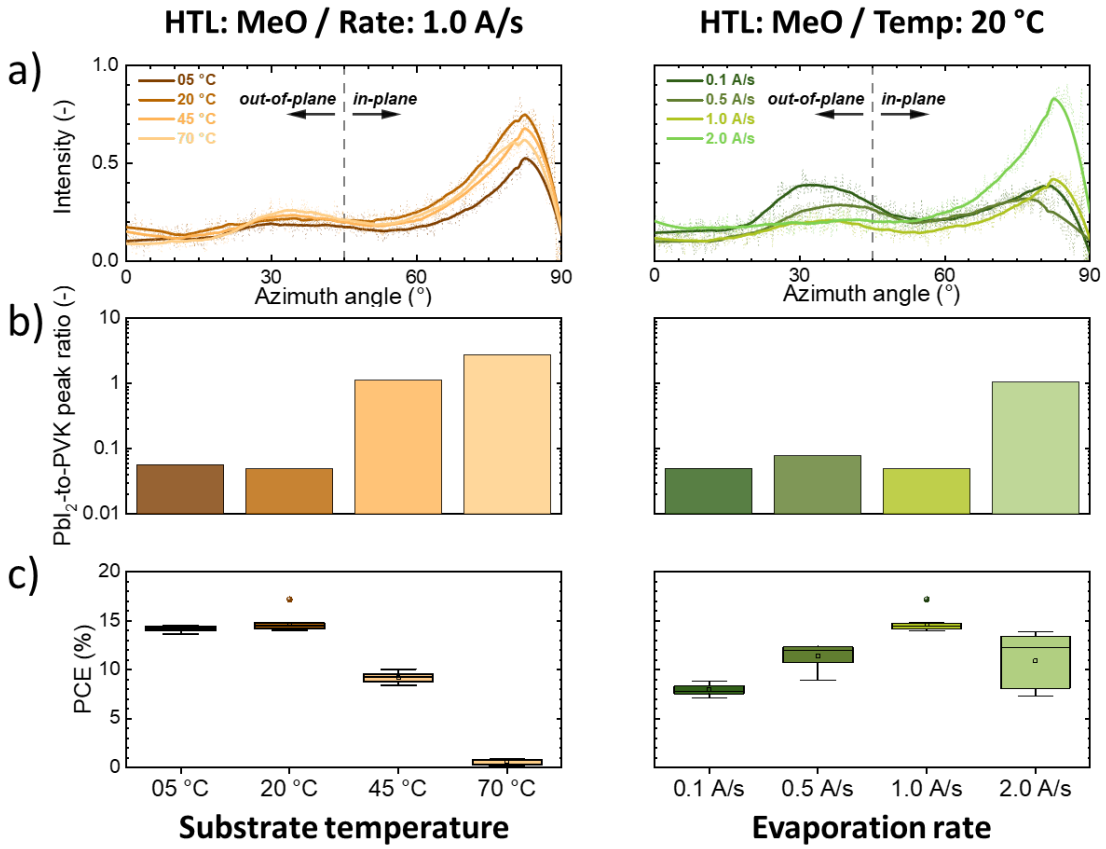

Figure 5: a) Pole figures from GIWAXS measurements for evaporated PbI_2 layers on MeO for different substrate temperatures and PbI_2 evaporation rates. b) XRD ratios of PbI_2 to perovskite peak intensities for perovskite films with same FAI to PbI_2 ratio and varying substrate temperature and evaporation rate of PbI_2 deposition. c) PCE statistics of final perovskite solar cells respectively

Supporting Information

The Supporting Information is available free of charge:

- Detailed Experimental Section, literature analysis for sequentially evaporated PSCs, additional solar cell efficiency data, EQE, MPP, SEM, XRD, GIWAXS.

Acknowledgements

The authors acknowledge the fruitful discussions with Bryce Richards and laboratory access to GIWAXS. In addition, the authors gratefully acknowledge the discussions with Richard Thelen and the laboratory access to AFM. This work was [partly] carried out with the support of the Karlsruhe Nano Micro Facility (KNMF, www.knmf.kit.edu), a Helmholtz Research Infrastructure at Karlsruhe Institute of Technology (KIT, www.kit.edu). The authors gratefully acknowledge financial support by the Helmholtz Association (project Zeitenwende, Solar Technology Acceleration Platform (Solar TAP), program-oriented funding period IV of the Helmholtz Association (Materials and Technologies for the Energy Transition, Topic 1: Photovoltaics and Wind Energy, Code: 38.01.02)), the Helmholtz Energy Materials Foundry, the German Federal Ministry for Economic Affairs and Climate Action (BMWK) through the project SHAPE (03EE1123A), and the Karlsruhe School of Optics and Photonics (KSOP). Funded by the European Union. Views and opinions expressed are however those of the author(s) only and do not necessarily reflect those of the European Union or RIA. Neither the European Union nor the granting authority can be held responsible for them. NEXUS project has received funding from the European Union's Horizon Europe research and innovation program under grant agreement No. 101075330.

References

(1) Filip, M. R.; Eperon, G. E.; Snaith, H. J.; Giustino, F. Steric Engineering of Metal-Halide Perovskites with Tunable Optical Band Gaps. *Nat Commun* **2014**, *5*. https://doi.org/10.1038/ncomms6757.

(2) Unger, E. L.; Kegelmann, L.; Suchan, K.; Sörell, D.; Korte, L.; Albrecht, S. Roadmap and Roadblocks for the Band Gap Tunability of Metal Halide Perovskites. *J Mater Chem A Mater* **2017**, *5* (23), 11401–11409. https://doi.org/10.1039/c7ta00404d.

(3) Stranks, S. D.; Eperon, G. E.; Grancini, G.; Menelaou, C.; Alcocer, M. J. P.; Leijtens, T.; Herz, L. M.; Petrozza, A.; Snaith, H. J. Electron-Hole Diffusion Lengths Exceeding 1 Micrometer in an Organometal Trihalide Perovskite Absorber. *Science* **2013**, *342* (6156), 341–344. https://doi.org/10.1126/science.1243982.

(4) De Wolf, S.; Holovsky, J.; Moon, S. J.; Löper, P.; Niesen, B.; Ledinsky, M.; Haug, F. J.; Yum, J. H.; Ballif, C. Organometallic Halide Perovskites: Sharp Optical Absorption Edge and Its Relation to Photovoltaic Performance. *Journal of Physical Chemistry Letters* **2014**, *5* (6), 1035–1039. https://doi.org/10.1021/jz500279b.

(5) Green, M. A.; Dunlop, E. D.; Yoshita, M.; Kopidakis, N.; Bothe, K.; Siefer, G.; Hinken, D.; Rauer, M.; Hohl-Ebinger, J.; Hao, X. Solar Cell Efficiency Tables (Version 64). *Progress in Photovoltaics: Research and Applications* **2024**, *32* (7), 425–441. https://doi.org/10.1002/pip.3831.

(6) *NREL Best Research-Cell Efficiency Chart, https://www.nrel.gov/pv/cell-efficiency.html, accessed: November 2024*.

(7) Howard, I. A.; Abzieher, T.; Hossain, I. M.; Eggers, H.; Schackmar, F.; Ternes, S.; Richards, B. S.; Lemmer, U.; Paetzold, U. W. Coated and Printed Perovskites for

Photovoltaic Applications. *Advanced Materials* **2019**, *31* (26), 1806702. https://doi.org/10.1002/adma.201806702.

(8) Jacobsson, T. J.; Hultqvist, A.; García-Fernández, A.; Anand, A.; Al-Ashouri, A.; Hagfeldt, A.; Crovetto, A.; Abate, A.; Ricciardulli, A. G.; Vijayan, A.; Kulkarni, A.; Anderson, A. Y.; Darwich, B. P.; Yang, B.; Coles, B. L.; Perini, C. A. R.; Rehermann, C.; Ramirez, D.; Fairen-Jimenez, D.; Di Girolamo, D.; Jia, D.; Avila, E.; Juarez-Perez, E. J.; Baumann, F.; Mathies, F.; González, G. S. A.; Boschloo, G.; Nasti, G.; Paramasivam, G.; Martínez-Denegri, G.; Näsström, H.; Michaels, H.; Köbler, H.; Wu, H.; Benesperi, I.; Dar, M. I.; Bayrak Pehlivan, I.; Gould, I. E.; Vagott, J. N.; Dagar, J.; Kettle, J.; Yang, J.; Li, J.; Smith, J. A.; Pascual, J.; Jerónimo-Rendón, J. J.; Montoya, J. F.; Correa-Baena, J.-P.; Qiu, J.; Wang, J.; Sveinbjörnsson, K.; Hirselandt, K.; Dey, K.; Frohna, K.; Mathies, L.; Castriotta, L. A.; Aldamasy, Mahmoud. H.; Vasquez-Montoya, M.; Ruiz-Preciado, M. A.; Flatken, M. A.; Khenkin, M. V.; Grischek, M.; Kedia, M.; Saliba, M.; Anaya, M.; Veldhoen, M.; Arora, N.; Shargaieva, O.; Maus, O.; Game, O. S.; Yudilevich, O.; Fassl, P.; Zhou, Q.; Betancur, R.; Munir, R.; Patidar, R.; Stranks, S. D.; Alam, S.; Kar, S.; Unold, T.; Abzieher, T.; Edvinsson, T.; David, T. W.; Paetzold, U. W.; Zia, W.; Fu, W.; Zuo, W.; Schröder, V. R. F.; Tress, W.; Zhang, X.; Chiang, Y.-H.; Iqbal, Z.; Xie, Z.; Unger, E. An Open-Access Database and Analysis Tool for Perovskite Solar Cells Based on the FAIR Data Principles. *Nat Energy* **2021**, *7* (1), 107–115. https://doi.org/10.1038/s41560-021-00941-3.

(9) Vaynzof, Y. The Future of Perovskite Photovoltaics—Thermal Evaporation or Solution Processing? *Adv Energy Mater* **2020**, *10* (48), 2003073. https://doi.org/10.1002/aenm.202003073.

(10) Abzieher, T.; Moore, D. T.; Roß, M.; Albrecht, S.; Silvia, J.; Tan, H.; Jeangros, Q.; Ballif, C.; Hoerantner, M. T.; Kim, B.-S.; Bolink, H. J.; Pistor, P.; Goldschmidt, J. C.; Chiang, Y.-H.; Stranks, S. D.; Borchert, J.; McGehee, M. D.; Morales-Masis, M.; Patel, J. B.; Bruno, A.; Paetzold, U. W. Vapor Phase Deposition of Perovskite Photovoltaics: Short Track to Commercialization? *Energy Environ Sci* **2024**, *17* (5), 1645–1663. https://doi.org/10.1039/D3EE03273F.

(11) Paliwal, A.; Zanoni, K. P. S.; Roldán-Carmona, C.; Hernández-Fenollosa, M. A.; Bolink, H. J. Fully Vacuum-Deposited Perovskite Solar Cells in Substrate Configuration. *Matter* **2023**, *6* (10), 3499–3508. https://doi.org/10.1016/j.matt.2023.07.011.

(12) Ritzer, D. B.; Abzieher, T.; Basibüyük, A.; Feeney, T.; Laufer, F.; Ternes, S.; Richards, B. S.; Bergfeld, S.; Paetzold, U. W. Upscaling of Perovskite Solar Modules: The Synergy of Fully Evaporated Layer Fabrication and All-laser-scribed Interconnections. *Progress in Photovoltaics: Research and Applications* **2022**, *30* (4), 360–373. https://doi.org/10.1002/pip.3489.

(13) Kosasih, F. U.; Erdenebileg, E.; Mathews, N.; Mhaisalkar, S. G.; Bruno, A. Thermal Evaporation and Hybrid Deposition of Perovskite Solar Cells and Mini-Modules. *Joule* **2022**, *6* (12), 2692–2734. https://doi.org/10.1016/j.joule.2022.11.004.

(14) Liu, M.; Johnston, M. B.; Snaith, H. J. Efficient Planar Heterojunction Perovskite Solar Cells by Vapour Deposition. *Nature* **2013**, *501* (7467), 395–398. https://doi.org/10.1038/nature12509.

(15) Susic, I.; Gil-Escrig, L.; Palazon, F.; Sessolo, M.; Bolink, H. J. Quadruple-Cation Wide-Bandgap Perovskite Solar Cells with Enhanced Thermal Stability Enabled by Vacuum Deposition. *ACS Energy Lett* **2022**, *7* (4), 1355–1363. https://doi.org/10.1021/acsenergylett.2c00304.

(16) Gil-Escrig, L.; Dreessen, C.; Palazon, F.; Hawash, Z.; Moons, E.; Albrecht, S.; Sessolo, M.; Bolink, H. J. Efficient Wide-Bandgap Mixed-Cation and Mixed-Halide Perovskite Solar Cells by Vacuum Deposition. *ACS Energy Lett* **2021**, *6* (2), 827–836. https://doi.org/10.1021/acsenergylett.0c02445.

(17) La-Placa, M. G.; Gil-Escrig, L.; Guo, D.; Palazon, F.; Savenije, T. J.; Sessolo, M.; Bolink, H. J. Vacuum-Deposited 2D/3D Perovskite Heterojunctions. *ACS Energy Lett* **2019**, *4* (12), 2893–2901. https://doi.org/10.1021/acsenergylett.9b02224.

(18) Gil-Escrig, L.; Dreessen, C.; Kaya, I. C.; Kim, B. S.; Palazon, F.; Sessolo, M.; Bolink, H. J. Efficient Vacuum-Deposited Perovskite Solar Cells with Stable Cubic FA1- XMAxPbI3. *ACS Energy Lett* **2020**, *5* (9), 3053–3061. https://doi.org/10.1021/acsenergylett.0c01473.

(19) Dewi, H. A.; Erdenebileg, E.; De Luca, D.; Mhaisalkar, S. G.; Bruno, A. Accelerated $MAPbI_3$ Co-Evaporation: Productivity Gains without Compromising Performance. *ACS Energy Lett* **2024**, *9* (9), 4319–4322. https://doi.org/10.1021/acsenergylett.4c01597.

(20) Li, H.; Tan, L.; Jiang, C.; Li, M.; Zhou, J.; Ye, Y.; Liu, Y.; Yi, C. Molten Salt Strategy for Reproducible Evaporation of Efficient Perovskite Solar Cells. *Adv Funct Mater* **2023**, *33* (10), 2211232. https://doi.org/10.1002/adfm.202211232.

(21) Gil-Escrig, L.; Susic, I.; Doğan, İ.; Zardetto, V.; Najafi, M.; Zhang, D.; Veenstra, S.; Sedani, S.; Arikan, B.; Yerci, S.; Bolink, H. J.; Sessolo, M. Efficient and Thermally Stable Wide Bandgap Perovskite Solar Cells by Dual-Source Vacuum Deposition. *Adv Funct Mater* **2023**, *33* (31), 2214357. https://doi.org/10.1002/adfm.202214357.

(22) Piot, M.; Alonso, J. E. S.; Zanoni, K. P. S.; Rodkey, N.; Ventosinos, F.; Roldán-Carmona, C.; Sessolo, M.; Bolink, H. Fast Coevaporation of 1 Mm Thick Perovskite Solar Cells. *ACS Energy Lett* **2023**, *8* (11), 4711–4713. https://doi.org/10.1021/acsenergylett.3c01724.

(23) Leyden, M. R.; Škorjanc, V.; Miaskiewicz, A.; Severin, S.; Maniyarasu, S.; Gries, T.; Beckedahl, J.; Scheler, F.; Simmonds, M.; Holzhey, P.; Kurpiers, J.; Korte, L.; Roß, M.; Albrecht, S. Loading Precursors into Self-Assembling Contacts for Improved Performance and Process Control in Evaporated Perovskite Solar Cells. *Solar RRL* **2024**, *2400575*. https://doi.org/10.1002/solr.202400575.

(24) Feeney, T.; Petry, J.; Torche, A.; Hauschild, D.; Hacene, B.; Wansorra, C.; Diercks, A.; Ernst, M.; Weinhardt, L.; Heske, C.; Gryn'ova, G.; Paetzold, U. W.; Fassl, P. Understanding and Exploiting Interfacial Interactions between Phosphonic Acid Functional Groups and Co-Evaporated Perovskites. *Matter* **2024**, *7* (6), 2066–2090. https://doi.org/10.1016/j.matt.2024.02.004.

(25) Castro-Méndez, A.-F.; Jahanbakhshi, F.; LaFollette, D. K.; Lawrie, B. J.; Li, R.; Perini, C. A. R.; Rappe, A. M.; Correa-Baena, J.-P. Tailoring Interface Energies via Phosphonic

Acids to Grow and Stabilize Cubic FAPbI _3 Deposited by Thermal Evaporation. *J Am Chem Soc* **2024**, *146* (27), 18459–18469. https://doi.org/10.1021/jacs.4c03911.

(26) Olthof, S.; Meerholz, K. Substrate-Dependent Electronic Structure and Film Formation of MAPbI 3 Perovskites. *Sci Rep* **2017**, *7*. https://doi.org/10.1038/srep40267.

(27) Abzieher, T.; Feeney, T.; Schackmar, F.; Donie, Y. J.; Hossain, I. M.; Schwenzer, J. A.; Hellmann, T.; Mayer, T.; Powalla, M.; Paetzold, U. W. From Groundwork to Efficient Solar Cells: On the Importance of the Substrate Material in Co-Evaporated Perovskite Solar Cells. *Adv Funct Mater* **2021**, *31* (42), 2104482. https://doi.org/10.1002/adfm.202104482.

(28) Roß, M.; Gil-Escrig, L.; Al-Ashouri, A.; Tockhorn, P.; Jošt, M.; Rech, B.; Albrecht, S. Co-Evaporated p-i-n Perovskite Solar Cells beyond 20% Efficiency: Impact of Substrate Temperature and Hole-Transport Layer. *ACS Appl Mater Interfaces* **2020**, *12* (35), 39261–39272. https://doi.org/10.1021/acsami.0c10898.

(29) Roß, M.; Severin, S.; Stutz, M. B.; Wagner, P.; Köbler, H.; Favin-Lévêque, M.; Al-Ashouri, A.; Korb, P.; Tockhorn, P.; Abate, A.; Stannowski, B.; Rech, B.; Albrecht, S. Co-Evaporated Formamidinium Lead Iodide Based Perovskites with 1000 h Constant Stability for Fully Textured Monolithic Perovskite/Silicon Tandem Solar Cells. *Adv Energy Mater* **2021**, *11* (35). https://doi.org/10.1002/aenm.202101460.

(30) Chen, C.; Kang, H.; Hsiao, S.; Yang, P.; Chiang, K.; Lin, H. Efficient and Uniform Planar-Type Perovskite Solar Cells by Simple Sequential Vacuum Deposition. *Advanced Materials* **2014**, *26* (38), 6647–6652. https://doi.org/10.1002/adma.201402461.

(31) Tavakoli, M. M.; Yadav, P.; Prochowicz, D.; Tavakoli, R.; Saliba, M. Multilayer Evaporation of MAFAPbI $_{3-x}$Cl $_x$ for the Fabrication of Efficient and Large-Scale Device Perovskite Solar Cells. *J Phys D Appl Phys* **2019**, *52* (3), 034005. https://doi.org/10.1088/1361-6463/aaebf1.

(32) Feng, J.; Jiao, Y.; Wang, H.; Zhu, X.; Sun, Y.; Du, M.; Cao, Y.; Yang, D.; Liu, S. (Frank). High-Throughput Large-Area Vacuum Deposition for High-Performance Formamidine-Based Perovskite Solar Cells. *Energy Environ Sci* **2021**, *14* (5), 3035–3043. https://doi.org/10.1039/D1EE00634G.

(33) Tavakoli, M. M.; Tavakoli, R. All-Vacuum-Processing for Fabrication of Efficient, Large-Scale, and Flexible Inverted Perovskite Solar Cells. *physica status solidi (RRL) – Rapid Research Letters* **2021**, *15* (1), 2000449. https://doi.org/10.1002/pssr.202000449.

(34) Li, H.; Zhou, J.; Tan, L.; Li, M.; Jiang, C.; Wang, S.; Zhao, X.; Liu, Y.; Zhang, Y.; Ye, Y.; Tress, W.; Yi, C. Sequential Vacuum-Evaporated Perovskite Solar Cells with More than 24% Efficiency. *Sci Adv* **2022**, *8* (28), eabo7422. https://doi.org/10.1126/sciadv.abo7422.

(35) Zhou, J.; Tan, L.; Liu, Y.; Li, H.; Liu, X.; Li, M.; Wang, S.; Zhang, Y.; Jiang, C.; Hua, R.; Tress, W.; Meloni, S.; Yi, C. Highly Efficient and Stable Perovskite Solar Cells via a Multifunctional Hole Transporting Material. *Joule* **2024**, *8* (6), 1691–1706. https://doi.org/10.1016/j.joule.2024.02.019.

(36) Yang, D.; Yang, Z.; Qin, W.; Zhang, Y.; Liu, S. (Frank); Li, C. Alternating Precursor Layer Deposition for Highly Stable Perovskite Films towards Efficient Solar Cells Using

Vacuum Deposition. *J Mater Chem A Mater* **2015**, *3* (18), 9401–9405. https://doi.org/10.1039/C5TA01824B.

(37) Tavakoli, M. M.; Yadav, P.; Prochowicz, D.; Tavakoli, R. Efficient, Hysteresis-Free, and Flexible Inverted Perovskite Solar Cells Using All-Vacuum Processing. *Solar RRL* **2021**, *5* (1), 2000552. https://doi.org/10.1002/solr.202000552.

(38) Tavakoli, M. M.; Simchi, A.; Mo, X.; Fan, Z. High-Quality Organohalide Lead Perovskite Films Fabricated by Layer-by-Layer Alternating Vacuum Deposition for High Efficiency Photovoltaics. *Mater Chem Front* **2017**, *1* (8), 1520–1525. https://doi.org/10.1039/C6QM00379F.

(39) Choi, Y.; Koo, D.; Jeong, M.; Jeong, G.; Lee, J.; Lee, B.; Choi, K. J.; Yang, C.; Park, H. Toward All-Vacuum-Processable Perovskite Solar Cells with High Efficiency, Stability, and Scalability Enabled by Fluorinated Spiro-OMeTAD through Thermal Evaporation. *Solar RRL* **2021**, *5* (9), 2100415. https://doi.org/10.1002/solr.202100415.

(40) Hsiao, S.; Lin, H.; Lee, W.; Tsai, W.; Chiang, K.; Liao, W.; Ren-Wu, C.; Chen, C.; Lin, H. Efficient All-Vacuum Deposited Perovskite Solar Cells by Controlling Reagent Partial Pressure in High Vacuum. *Advanced Materials* **2016**, *28* (32), 7013–7019. https://doi.org/10.1002/adma.201601505.

(41) Ng, A.; Ren, Z.; Shen, Q.; Cheung, S. H.; Gokkaya, H. C.; Bai, G.; Wang, J.; Yang, L.; So, S. K.; Djurišić, A. B.; Leung, W. W.; Hao, J.; Chan, W. K.; Surya, C. Efficiency Enhancement by Defect Engineering in Perovskite Photovoltaic Cells Prepared Using Evaporated PbI_2 /CH_3NH_3I Multilayers. *J Mater Chem A Mater* **2015**, *3* (17), 9223–9231. https://doi.org/10.1039/C4TA05070C.

(42) Lin, D.; Gao, Y.; Zhang, T.; Zhan, Z.; Pang, N.; Wu, Z.; Chen, K.; Shi, T.; Pan, Z.; Liu, P.; Xie, W. Vapor Deposited Pure A-$FAPbI_3$ Perovskite Solar Cell via Moisture-Induced Phase Transition Strategy. *Adv Funct Mater* **2022**, *32* (48), 2208392. https://doi.org/10.1002/adfm.202208392.

(43) Lin, D.; Fang, J.; Yang, X.; Wang, X.; Li, S.; Wang, D.; Xie, G.; Li, H.; Wang, X.; Qiu, L. Modulating the Distribution of Formamidinium Iodide by Ultrahigh Humidity Treatment Strategy for High-Quality Sequential Vapor Deposited Perovskite. *Small* **2024**, *20* (12), 2307960. https://doi.org/10.1002/smll.202307960.

(44) Zou, S.; Liang, S.; Yu, T.; Su, J.; Jiang, Y.; Hua, R.; Huang, Z.; Zhang, W.; Shi, L.; Guo, Y.; Dong, Q.; Han, Y.; Ma, H.; Gao, Y.; Shi, Y.; Dong, Y. Scalable Large Area Perovskite Solar Cell Modules Fabricated with High Humidity Tolerance by Vacuum Deposition. *Mater Today Energy* **2024**, *40*, 101506. https://doi.org/10.1016/j.mtener.2024.101506.

(45) Smecca, E.; Valenzano, V.; Valastro, S.; Deretzis, I.; Mannino, G.; Malandrino, G.; Accorsi, G.; Colella, S.; Rizzo, A.; La Magna, A.; Listorti, A.; Alberti, A. Two-Step MAPbI 3 Deposition by Low-Vacuum Proximity-Space-Effusion for High-Efficiency Inverted Semitransparent Perovskite Solar Cells. *J Mater Chem A Mater* **2021**, *9* (30), 16456–16469. https://doi.org/10.1039/D1TA02535J.

(46) Mei, A.; Sheng, Y.; Ming, Y.; Hu, Y.; Rong, Y.; Zhang, W.; Luo, S.; Na, G.; Tian, C.; Hou, X.; Xiong, Y.; Zhang, Z.; Liu, S.; Uchida, S.; Kim, T. W.; Yuan, Y.; Zhang, L.; Zhou, Y.; Han, H. Stabilizing Perovskite Solar Cells to IEC61215:2016 Standards with over 9,000-h

Operational Tracking. *Joule* **2020**, *4* (12), 2646–2660. https://doi.org/10.1016/j.joule.2020.09.010.

(47) Kang, Y.; Wang, A.; Li, R.; Song, Y.; Wang, X.; Li, H.; Xu, W.; Zhang, L.; Dong, Q. Thermal Shock Fabrication of Ion-Stabilized Perovskite and Solar Cells. *Advanced Materials* **2022**, *34* (32). https://doi.org/10.1002/adma.202203166.

(48) Al-Ashouri, A.; Magomedov, A.; Roß, M.; Jošt, M.; Talaikis, M.; Chistiakova, G.; Bertram, T.; Márquez, J. A.; Köhnen, E.; Kasparavičius, E.; Levcenco, S.; Gil-Escrig, L.; Hages, C. J.; Schlatmann, R.; Rech, B.; Malinauskas, T.; Unold, T.; Kaufmann, C. A.; Korte, L.; Niaura, G.; Getautis, V.; Albrecht, S. Conformal Monolayer Contacts with Lossless Interfaces for Perovskite Single Junction and Monolithic Tandem Solar Cells. *Energy Environ Sci* **2019**, *12* (11), 3356–3369. https://doi.org/10.1039/c9ee02268f.

(49) Li, Z.; Li, B.; Wu, X.; Sheppard, S. A.; Zhang, S.; Gao, D.; Long, N. J.; Zhu, Z. Organometallic-Functionalized Interfaces for Highly Efficient Inverted Perovskite Solar Cells. *Science* **2022**, *376* (6591), 416–420. https://doi.org/10.1126/science.abm8566.

(50) Abzieher, T.; Moore, D. T.; Roß, M.; Albrecht, S.; Silvia, J.; Tan, H.; Jeangros, Q.; Ballif, C.; Hoerantner, M. T.; Kim, B.-S.; Bolink, H. J.; Pistor, P.; Goldschmidt, J. C.; Chiang, Y.-H.; Stranks, S. D.; Borchert, J.; McGehee, M. D.; Morales-Masis, M.; Patel, J. B.; Bruno, A.; Paetzold, U. W. Vapor Phase Deposition of Perovskite Photovoltaics: Short Track to Commercialization? *Energy Environ Sci* **2024**. https://doi.org/10.1039/D3EE03273F.

(51) Wang, S.; Tan, L.; Zhou, J.; Li, M.; Zhao, X.; Li, H.; Tress, W.; Ding, L.; Graetzel, M.; Yi (易陈谊), C. Over 24% Efficient MA-Free CsxFA1−xPbX3 Perovskite Solar Cells. *Joule* **2022**, *6* (6), 1344–1356. https://doi.org/10.1016/j.joule.2022.05.002.

(52) Heinze, K. L.; Schulz, T.; Scheer, R.; Pistor, P. Structural Evolution of Sequentially Evaporated (Cs,FA)Pb(I,Br) $_3$ Perovskite Thin Films via In Situ X-Ray Diffraction. *physica status solidi (a)* **2024**, *221* (3), 2300690. https://doi.org/10.1002/pssa.202300690.

(53) Farag, A.; Feeney, T.; Hossain, I. M.; Schackmar, F.; Fassl, P.; Küster, K.; Bäuerle, R.; Ruiz-Preciado, M. A.; Hentschel, M.; Ritzer, D. B.; Diercks, A.; Li, Y.; Nejand, B. A.; Laufer, F.; Singh, R.; Starke, U.; Paetzold, U. W. Evaporated Self-Assembled Monolayer Hole Transport Layers: Lossless Interfaces in p-i-n Perovskite Solar Cells. *Adv Energy Mater* **2023**, *13* (8). https://doi.org/10.1002/aenm.202203982.

(54) Gao, Y.; Raza, H.; Zhang, Z.; Chen, W.; Liu, Z. Rethinking the Role of Excess/Residual Lead Iodide in Perovskite Solar Cells. *Adv Funct Mater* **2023**, *33* (26), 2215171. https://doi.org/10.1002/adfm.202215171.

(55) Kalasariya, N.; Alexander, A.; Bhunia, P. K.; Gutierrez-Partida, E.; Benny, R.; Stolterfoht, M.; Namboothiry, M. A. G. Controlling Lead Halide Residue in Perovskite Solar Cells: A Method to Improve the Photostability and Hysteresis. *Solar RRL* **2024**, *8* (1), 2300788. https://doi.org/10.1002/solr.202300788.

(56) Susic, I.; Zanoni, K. P. S.; Paliwal, A.; Kaya, I. C.; Hawash, Z.; Sessolo, M.; Moons, E.; Bolink, H. J. Intrinsic Organic Semiconductors as Hole Transport Layers in p–i–n Perovskite Solar Cells. *Solar RRL* **2022**, *6* (4), 2100882. https://doi.org/10.1002/solr.202100882.

(57) Stolterfoht, M.; Caprioglio, P.; Wolff, C. M.; Márquez, J. A.; Nordmann, J.; Zhang, S.; Rothhardt, D.; Hörmann, U.; Amir, Y.; Redinger, A.; Kegelmann, L.; Zu, F.; Albrecht, S.; Koch, N.; Kirchartz, T.; Saliba, M.; Unold, T.; Neher, D. The Impact of Energy Alignment and Interfacial Recombination on the Internal and External Open-Circuit Voltage of Perovskite Solar Cells. *Energy Environ Sci* **2019**, *12* (9), 2778–2788. https://doi.org/10.1039/C9EE02020A.

(58) Parrott, E. S.; Patel, J. B.; Haghighirad, A.-A.; Snaith, H. J.; Johnston, M. B.; Herz, L. M. Growth Modes and Quantum Confinement in Ultrathin Vapour-Deposited MAPbI 3 Films. *Nanoscale* **2019**, *11* (30), 14276–14284. https://doi.org/10.1039/C9NR04104D.

(59) Pesch, R.; Diercks, A.; Petry, J.; Welle, A.; Pappenberger, R.; Schackmar, F.; Eggers, H.; Sutter, J.; Lemmer, U.; Paetzold, U. W. Hybrid Two-Step Inkjet-Printed Perovskite Solar Cells. *Solar RRL* **2024**, *8* (13), 2100882. https://doi.org/10.1002/solr.202400165.

(60) Nguyen, V. S.; Zimmermann, I.; Grépin, E.; Medjoubi, K.; Jutteau, S.; Donsanti, F.; Bruhat, E.; Duchatelet, A.; Berson, S.; Rousset, J. Solvent-Vapor Assisted Conversion Process for Hybrid Perovskites Coupling Thermal Evaporation and Slot-Die Coating. *Mater Sci Semicond Process* **2023**, *158*, 107358. https://doi.org/10.1016/j.mssp.2023.107358.

(61) Steele, J. A.; Solano, E.; Hardy, D.; Dayton, D.; Ladd, D.; White, K.; Chen, P.; Hou, J.; Huang, H.; Saha, R. A.; Wang, L.; Gao, F.; Hofkens, J.; Roeffaers, M. B. J.; Chernyshov, D.; Toney, M. F. How to GIWAXS: Grazing Incidence Wide Angle X-Ray Scattering Applied to Metal Halide Perovskite Thin Films. *Adv Energy Mater* **2023**, *13* (27), 2300760. https://doi.org/10.1002/aenm.202300760.

(62) Jiang, D.; Liu, Z.; Li, J.; Cao, H.; Qian, Y.; Ren, Z.; Zhang, S.; Qiu, Y.; Zhang, C.; Wei, J.; Yang, L.; Yin, S. Non-Laser and All-Vapor-Phase Processed Perovskite Solar Modules Stabilized by Naturally Formed Barrier Layers. *Joule* **2024**, *8* (4), 1161–1175. https://doi.org/10.1016/j.joule.2024.02.007.

(63) Zhang, J.; Ji, X.; Wang, X.; Zhang, L.; Bi, L.; Su, Z.; Gao, X.; Zhang, W.; Shi, L.; Guan, G.; Abudula, A.; Hao, X.; Yang, L.; Fu, Q.; Jen, A. K.-Y.; Lu, L. Efficient and Stable Inverted Perovskite Solar Modules Enabled by Solid–Liquid Two-Step Film Formation. *Nanomicro Lett* **2024**, *16* (1), 190. https://doi.org/10.1007/s40820-024-01408-2.

(64) Li, Z.; Li, J.; Cao, H.; Qian, Y.; Zhai, J.; Qiu, Y.; Yang, L.; Yin, S. Surface-Orientation Elimination of Vapor-Deposited PbI_2 Flakes for Efficient Perovskite Synthesis on Curved Solar Cells. *ACS Appl Mater Interfaces* **2021**, *13* (38), 45496–45504. https://doi.org/10.1021/acsami.1c12283.

(65) Liu, A.; Liu, K.; Zhou, H.; Li, H.; Qiu, X.; Yang, Y.; Liu, M. Solution Evaporation Processed High Quality Perovskite Films. *Sci Bull* **2018**, *63* (23), 1591–1596. https://doi.org/10.1016/j.scib.2018.11.004.

(66) Tan, L.; Zhou, J.; Zhao, X.; Wang, S.; Li, M.; Jiang, C.; Li, H.; Zhang, Y.; Ye, Y.; Tress, W.; Ding, L.; Grätzel, M.; Yi, C. Combined Vacuum Evaporation and Solution Process for High-Efficiency Large-Area Perovskite Solar Cells with Exceptional Reproducibility. *Advanced Materials* **2023**, *35* (13), 2205027. https://doi.org/10.1002/adma.202205027.